Boosting electrochemical conversion of CO_2 to ethanol through the confinement of pyridinic N-B layer on copper nanoparticles

Yuying Zhao [a,b,c], Qixin Yuan [b], Ruting Xu [a], Chenhao Zhang [d], Kang Sun [a], Ao Wang [a], Anqi Zhang [e], Ziyun Wang [c,*], Jianchun Jiang [a,b,**], Mengmeng Fan [a,b,**]

[a] Key Lab of Biomass Energy and Material, Jiangsu Province, Jiangsu Co-Innovation Center of Efficient Processing and Utilization of Forest Resources, Institute of Chemical Industry of Forest Products, Chinese Academy of Forestry, Nanjing 210042, China
[b] Jiangsu Co-Innovation Center of Efficient Processing and Utilization of Forest Resources, International Innovation Center for Forest Chemicals and Materials, College of Chemical Engineering, Nanjing Forestry University, Nanjing 210037, China
[c] School of Chemical Sciences, University of Auckland, Auckland 1010, New Zealand
[d] Shanghai Key Laboratory of Rare Earth Functional Materials and Education Ministry Key Laboratory of Resource Chemistry, Shanghai Normal University, Shanghai 200234, China
[e] School of Chemical Engineering, Tianjin University, Tianjin 30072, China

ARTICLE INFO

ABSTRACT

Developing efficient electrocatalysts for CO_2 reduction has gained significant attention in the field of sustainable energy, especially the Cu-based catalysts for CO_2 conversion to valuable alcohols. In this study, we developed Cu nanoparticles supported on pyridinic N-B doped graphene nanoribbons/amorphous carbon (Cu/BNC-1) as an electrocatalyst for CO_2 reduction, exhibiting substantially improved ethanol (EtOH) conversion rate in terms of activity, selectivity, and stability. The Cu/BNC-1 achieved a remarkable 58.64 % Faradaic efficiency (FE) for producing EtOH at -1.0 V vs. RHE with a current density of 20.4 mA cm^{-2} in 0.5 M KHCO$_3$ electrolyte. In-situ Raman, FT-IR, and density functional theory (DFT) calculations demonstrated that the high C_{2+} product selectivity of Cu/BNC-1 attributed to the pyridinic N-B modulation, lowering the CO dimerization barrier. Moreover, the synergistic confinement effect of Cu and BNC can stabilize the C-O bond of the *HOCCH intermediate, thereby increasing the yield of EtOH.

1. Introduction

Electrochemical carbon dioxide reduction reaction (CO_2RR) with renewable electricity to valuable chemicals or fuels is one widely accepted promising approach to alleviate the greenhouse effect and store chemical energy. Under the effect of catalysts, the complicated CO_2RR reaction pathways produce various hydrocarbons and oxygenated compounds with C_1 (e.g., CH_4 [1], HCOOH [2], CO [3]), C_2 (e.g., C_2H_4 [4], C_2H_6 [5], EtOH [6]) or C_{2+} products (e.g., n-C_3H_7OH [7]). Among various multiple-carbon products, EtOH is one more promising liquid fuel because of its wide application, high energy density, facile separation, storage, and convenient transport [8]. To achieve high Faradaic efficiency (FE) and high partial current density in producing EtOH, apart from completive hydrogen evolution reaction (HER), the

great challenge is derived from the intrinsic catalytic selectivity of electrocatalysts [6,9].

Currently, Cu-based catalysts can convert CO_2 toward EtOH via coupling *CO intermediates by many modulating strategies for Cu nanostructure (e.g., morphology, facet, vacancy, dopant) [10–13]. Optimizing the electronic structure of Cu catalyst to effectively regulate the adsorption of key intermediates (*H, *COOH, and *CO) is beneficial to enhance the C-C coupling pathway for multi-carbon products. For the 12-electron products, ethylene is the competing C_2 product with EtOH. Compared to ethylene produced on pure Cu catalysts, the EtOH showed a more saturated structure for the intermediates *HCCOH, leading to lower stability of further hydrogenated intermediates [14]. Moreover, pure Cu catalysts exhibit several limitations in the CO_2RR, including a tendency for particle agglomeration, which diminishes the surface area

and the accessibility of active sites. The pure Cu catalysts also suffer from poor durability due to dissolution, corrosion, or morphological transformations under prolonged operational conditions. Additionally, these catalysts often lack specificity, leading to a diverse array of products rather than a desired singular output. Furthermore, the pure Cu catalysts necessitate high overpotentials, escalating energy requirements and detracting from the process's energy efficiency. Consequently, more accurate modulation for pure Cu catalyst was required to achieve high FE of EtOH with long-term stability.

Compared to pure Cu catalysts, carbon supported Cu catalyst is one typical structure for highly efficient electrocatalyst, for example, single metal atoms dispersed on N-doped carbon materials, which have the advantage of enhanced conductivity, stability and metal utilization rate [3,10,15]. Molecular metal-nitrogen-carbon (M-N-C), especially dual atom catalysts (DACs), have· garnered significant interest in the fields of CO_2RR due to their potential environmental benefits [16–18]. Su et al. reported CNTs were ideal substrates for inducing optimum properties through molecular curvature [19]. CoPc/SWCNTs achieved methanol partial current densities higher than 90 mA cm^{-2} in CO_2RR with selectivity exceeding 60 %. Moreover, there are more facile modulating strategies for the electronic structure of Cu catalyst by the synergistic effect of heteroatom dopant on the carbon matrix [9,14]. Therefore, many researchers began to focus on the design of carbon support to modulate Cu catalysts. It's a promising route to achieve excellent CO_2 electrocatalyst by combining various carbon substrate modulation (e.g., pore distribution, defect engineering, heteroatom doping) and Cu modulation (e.g., morphology, facet, vacancy, dopant). The carbon supports not only modulated the key catalytic sites of Cu but also provided many sites to catalytically produce CO products [20,21], the more ideal precursor to synthesize EtOH. For example, CuO clusters supported on N-doped carbon nanosheets for producing EtOH with FE of 51 % with a partial current density of 14.4 mAcm^{-2} at −1.1 V vs. RHE [6], N-doped graphene quantum dots on Cu nanorods for producing C_{2+} alcohols with 52.4 % FE [22], single-atom Cu on N-doped carbon for producing EtOH with FE of 55 % under optimized conditions in 0.1 M CsHCO$_3$ at −1.2 V vs. RHE [23]. The carbon supported or mixed Cu catalysts still showed low stability. Challenges with carbon materials modulating Cu encompass uneven distribution of Cu particles, difficulties in finely adjusting Cu-carbon interactions, and inconsistent control over Cu size and shape. These issues can significantly impact the catalyst activity, selectivity, and stability. Therefore, it is urgent to explore the structure-activity relationship between various carbon nanostructure, dopant configuration and the Cu electronic structure to achieve high FE and partial current density in producing EtOH.

Here we fabricated Cu nanoparticles supported on pyridinic N-B doped graphene nanoribbons/amorphous carbon structure (Cu/BNC-1) as the electrocatalyst for CO_2RR, achieving greatly enhanced EtOH conversion rate in terms of activity, selectivity and stability. The Cu/BNC-1 showed high EtOH FE of 58.64 % at the potential of −1.0 V vs. RHE with a current density 20.4 mA cm^{-2} in 0.5 M KHCO$_3$ electrolyte. The Cu/BNC-1 showed great long-term durability over 24 h with retaining FE of 55 %. The enhanced catalytic performance of Cu/BNC-1 to EtOH is superior to the reported carbon-supported Cu catalysts. The evolution of Cu nanoparticles during long-term durability revealed the modulating effect of pyridinic N-B sites on the Cu electronic structure. The in-situ Raman, FT-IR and theoretical calculations presented the structure-activity relationship between EtOH selectivity and the system of Cu/heteroatom doped carbon support.

2. Experimental and computational methods

2.1. Chemicals

Chitosan ($C_{56}H_{103}N_9O_{39}$), boric acid, Copper (II) chloride (CuCl$_2$·2H$_2$O), melamine, hydrochloric acid (HCl, 37 %), and iron nitrate (Fe (NO$_3$)$_3$·9H$_2$O) were purchased from Aladdin Group. All

chemicals were of analytical grade as received. Nafion solution (5 wt%) was purchased from DuPont.

2.2. Materials synthesis

BNC-1 was synthesized though a one-pot "double-catalysts" strategy, chitosan, boric acid and iron nitrate acting as carbon source nitrogen source, boron source and catalyst respectively. In a typical synthesis, 10 g ferric nitrate was weighed and dispersed in distilled water, 4 g chitosan was added and dispersed in 300 mL H$_3$BO$_3$ (1 M). The solution was heated with stirring at 80 °C for 2 h and then the resulting mixed gelatinous mass was completely dried in an oven at 120 °C. The resulting powder was heated to 800°C at 2°C min^{-1} under N$_2$ atmosphere and kept in a quartz tube furnace for 10 h. This was followed by ultrasonic washing with 1 M HCl to remove inorganic Fe and H$_3$BO$_3$ and washing with deionized water to neutrality to obtain BNC-1. The synthesis approaches for BNC-2 were the same as BNC-1 without iron nitrate.

For Cu/BNC-1, 2 g BNC-1, 500 mg melamine, 200 mg CuCl$_2$·2H$_2$O, 10 mL ethanol and 10 mL water were added into a 50 mL bottle. The mixture was stirred for 24 h at room temperature and then centrifuged. The sample obtained by centrifugation was dried in a vacuum oven at 60°C for 24 h and ground thoroughly. Finally, the sample was heated to 550 °C at 8 °C min^{-1} and maintained for 4 h in H$_2$/Ar flow (5 vol% H$_2$ in Ar). After that, the sample was collected after cooling to room temperature. The preparing processes of Cu/BNC-2 was same to Cu/BNC-1, except for the replacement of BNC-1 by BNC-2. The preparing processes of CuN$_4$ was same to Cu/BNC-1, except no BNC-1.

2.3. Characterization

High-Resolution Transmission Electron Microscope (HR-TEM) was performed on a FEI Talos F200 at an accelerating voltage of 200 kV. N$_2$ adsorption-desorption isotherm tests were carried out on a gas adsorption analyzer (ASAP2460, Micromeritics). The structure and chemical composition of the samples were characterized by X-ray diffraction (XRD, D8 Focus Germany, Bruker), X-ray photoelectron spectroscopy (XPS, Thermo Fisher Nexsa), fourier transform infrared (FTIR, Nicolet iS10 spectrophotometer), Raman spectra (Thermofisher Scientific DXR2xi). In situ Raman and FTIR measurements were carried out using a Renishaw in Via Raman microscope in a modified flow cell with a water immersion objective.

2.4. Electrochemical measurements

All the electrochemical measurements were carried out on a CHI 760E (CH Instrument, Shanghai) electrochemical workstation. As mentioned above, the geometric size of working electrodes was 1 cm × 1 cm. In a H-cell, the counter and reference electrodes were Pt foil and Ag/AgCl electrode with an inner solution containing saturated KCl, respectively. Proton exchange membrane (DuPont Nafion 117) was used as the separator between the anode and cathodic chambers, and the CO$_2$ flow rate was 20 sccm. In the commercial flow cell, the gas diffusion electrode, Ni foam, anion exchange membrane (Fumasep FAA-3-PK-130) were used. The reference electrode was an Ag/AgCl electrode with an inner solution containing saturated KCl. CO$_2$, catholyte and anolyte flow rates were 20 sccm, 20 mL min^{-1} and 80 mL min^{-1}, respectively. The catalyst inks were prepared by homogeneously dispersing the catalyst (10 mg) in a solution containing isopropanol (800 μL), DI water (180 μL), and Nafion solution (20 μL). All the tests were performed in a CO$_2$-saturated 0.5 M KHCO$_3$ electrolyte (pH 7.2) or in a N$_2$-saturated 0.5 M KHCO$_3$ electrolyte (pH 8.3) with a rate of 20 sccm. The initially measured potentials were transformed to the reversible hydrogen electrode (RHE) based on the Nernst equation: E (RHE) = E (Ag/AgCl) + 0.199 + 0.059 × pH.

2.5. Product quantifications

For the FE analysis, the gas products were detected by an online gas chromatograph (GC, Shimadzu GC 2014) equipped with a thermal conductivity detector (TCD) for H_2 quantification and a flame ionization detector (FID) for CH_4, CO, C_2H_4 quantification. The liquid products

were detected by nuclear magnetic resonance (NMR; Bruker Avance III HD 600 MHz NMR).

2.6. Computational details

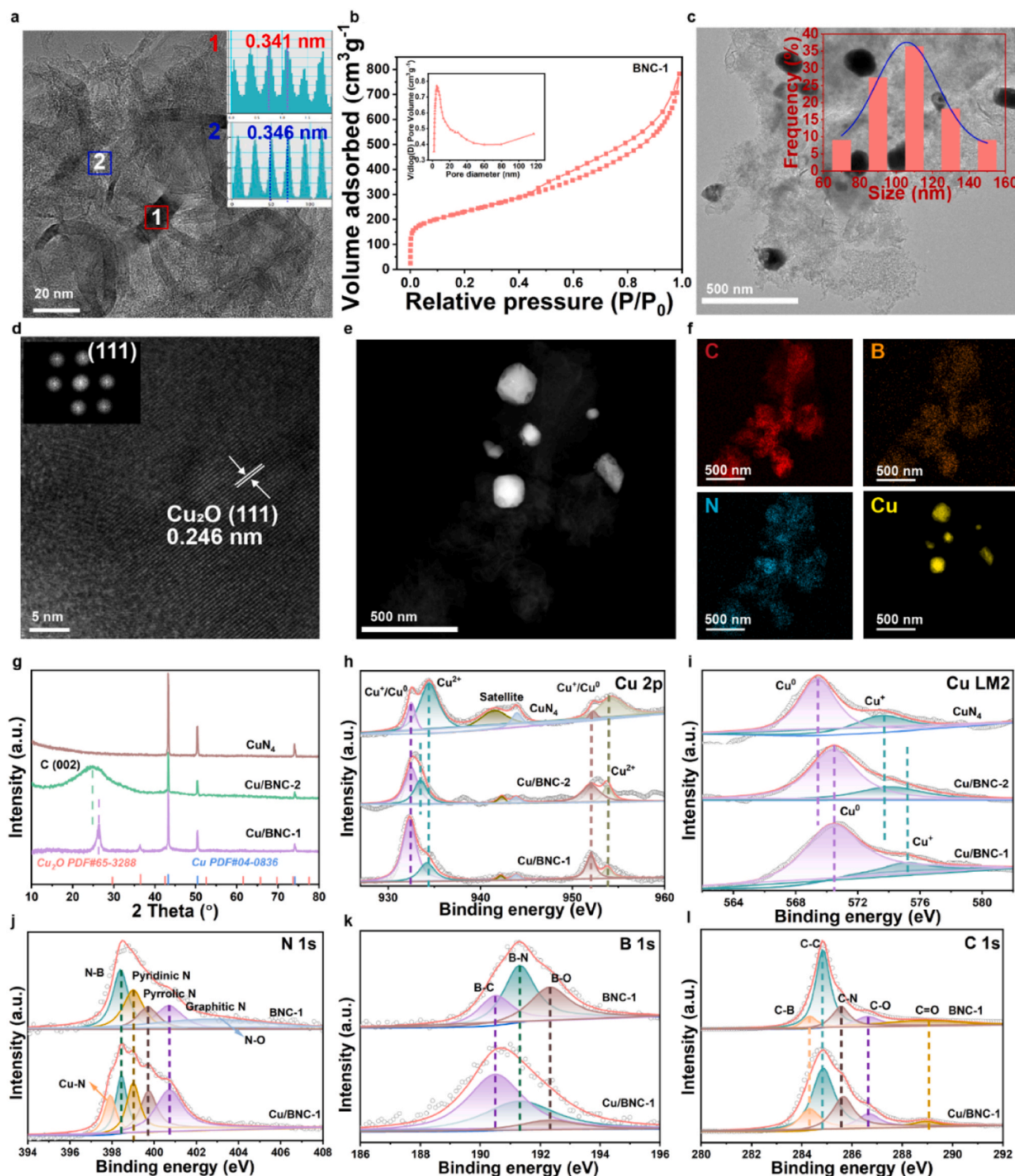Our computational simulations were performed with the Vienna ab

Fig. 1. (a) TEM images of BNC-1 (inset: corresponding lattice fringes of selected area 1 and 2). (b) N_2 adsorption-desorption isotherms of BNC-1 (inset, the corresponding pore size distribution). (c) TEM images of Cu/BNC-1 (inset: corresponding particle size distribution). (d) HR-TEM images of Cu/BNC-1 (inset: the corresponding Cu_2O lattice fringes). (e, f) The HAADF-STEM image of Cu/BNC-1 and the corresponding element mapping images of C (red), B (orange), N (blue) and Cu (yellow). (g) XRD patterns. (h) Cu 2p XPS spectra. (i) Cu LM2 XPS spectra of Cu/BN-C-1, Cu/BNC-2 and CuN4. (j) N 1 s XPS spectrum. (k) B 1 s XPS spectrum. (l) C 1 s XPS spectrum of Cu/BNC-1 and BNC-1.

initio simulation package (VASP) with the projector augmented wave (PAW) method to describe the interaction between atomic cores and valence electrons with DFT [24]. The Perdew-Burke-Ernzerhof (PBE) functional within the generalized gradient approximation (GGA) was used to implement DFT calculations, The van der Waals effects are included in the computations by using Grimme DFT-D3 method [25]. The computational hydrogen electrode (CHE) was used to calculate the free energy of each intermediate state. The free energy of a chemical reaction is calculated by $\Delta Gn = \Delta En - T\Delta S + \Delta ZPE$, where ΔEn is DFT-calculated reaction energy in explicit solvent, $T\Delta S$ is the entropy contributions to reaction at T = 298.15 K, ΔZPE is zero-point energy (ZPE) correction based on the calculated vibrational frequencies [26, 27].

3. Results and discussion

3.1. Synthesis and characterization of Cu/BNC-1

We first fabricated abundant pyridinic N-B species doped porous carbon matrix with the hierarchical structure of graphene nanoribbons/amorphous carbon (BNC-1) by our reported approach [28]. Then, Cu nanoparticles were loaded on the porous BNC-1 through post chemical impregnation process followed by annealing treatment under H_2/Ar atmosphere. The control carbon supports with co-doping B, N atoms (without pyridinic N-B sites), and the corresponding carbon-supported Cu catalysts were defined as Cu/BNC-2. N-doped carbon supported Cu catalyst was defined as CuN_4 prepared by annealing the precursors of melamine and $CuCl_2$. As shown in the high-resolution transmission electron microscopy (HR-TEM) image in Fig. 1a, the BNC-1 showed porous amorphous carbon interspersed with abundant graphene nanoribbons while the BNC-2 just showed amorphous structure (Fig. S1). Fe$(NO_3)_3 \cdot 9 H_2O$ additives were observed to promote the graphitization in BNC-1 and facilitate the formation of crystal graphene nanoribbons, enhancing material conductivity and structural integrity. The high specific surface area of 800 $m^2 g^{-1}$ and abundant mesopores (pore diameter distribution of 2–20 nm) made BNC-1 as promising carbon support to Cu catalyst measured by the N_2 adsorption–desorption isotherms (Fig. 1b). In the high-resolution transmission electron microscopy (HR-TEM) image of Cu/BNC-1, we observed Cu nanoparticles were dispersed on amorphous carbon matrix and the diameter size of Cu nanoparticles was located at ~100 nm in Fig. 1c. Cu nanoparticles within both Cu/BNC-2 (Fig. S2) and Cu/BNC-1 approximate 100 nm in diameter size, suggesting a consistent nanoparticle dimension across these samples. The surface of Cu nanoparticles displayed the typical crystalline lattice distance of 0.246 nm (Fig. 1d), corresponding to the (111) facet of Cu_2O with the typical fast Fourier transform (FFT) diffraction pattern (Fig. 1d, inset) [29]. The High angle annular dark-field scanning transmission electron microscopy (HAADF-STEM) image and corresponding B, N, Cu mappings by Energy Dispersive Spectrometer (EDS) confirmed the uniform distribution of pyridinic N-B species on carbon matrix, and the predominant structure of Cu nanoparticles (Fig. 1e, f). The ICP-MS results (Table S1) confirmed that the Cu concentrations in Cu/BNC-1 and Cu/BNC-2 were consistent, effectively ruling out variations in Cu content as a factor in their catalytic performance differences.

In X-ray diffraction (XRD) patterns, apart from the typical (111) plane of Cu_2O at 36.3°, the Cu/BNC-1 also displayed the distinctly typical Cu^0 peaks of (111) and (200) planes at 43.2° and 50.4° belonging to a metallic Cu^0 (PDF#04–0836) in Fig. 1g, respectively, indicating that the core-shell structure of Cu_2O layer covering Cu^0 core. Compared to the Cu/BNC-1, the Cu/BNC-2 and CuN_4 only exhibited the typical peaks of Cu^0, indicating the BNC-1 support was beneficial to stabilizing the Cu^+ via abundant pyridinic N-B sites. All the high-resolution Cu 2p spectra obtained by X-ray photoelectron spectroscopy (XPS) can be fitted into two subpeaks, and the dominant subpeaks at lower and higher binding energy can be assigned to Cu^0/Cu^+ and Cu^{2+} in Fig. 1h,

respectively. Compared to the Cu/BNC-2, the Cu/BNC-1 has the enhanced Cu^0/Cu^+ peak intensity, which can be attributed to the Cu_2O coverage on Cu nanoparticles. Compared to the Cu/BNC-2 (932.7 eV) and Cu/NC (932.7 eV), the Cu^0/Cu^+ peak of Cu/BNC-1 moved to lower binding energy at 932.3 eV, indicating an increasing valence state of Cu in the catalysts [13]. Moreover, in Auger electron spectroscopy (AES) of Cu LM2 spectra (Fig. 1i), the Cu/BNC-1 showed the Cu nanoparticle mainly consisted of a Cu^+ (Cu_2O) oxidation state near 569.8 eV, while the Cu peak of Cu/BNC-2 was shifted into higher binding energy at 570.4 eV demonstrating higher Cu oxidation state due to easy oxidation of surface Cu^0 species [29,30]. As reported in our previous research [31–34], the high-resolution N1s of BNC-1 can be deconvoluted into five peaks corresponding to pyridinic N-B at 398.4 eV, pyridinic N at 399.0 eV, pyrrolic N at 399.7 eV, graphitic N at 400.7 eV, and N-O at 402.9 eV in Fig. 1j, respectively. Remarkably, the new peak of Cu-N at appears in the Cu/BNC-1, indicating the effective immobilization of Cu nanoparticles on carbon matrix by general N-metal bonding (Fig. 1j). To the contrary, there was little pyridinic N-B species in the BNC-2 and Cu/BNC-2 as demonstrated by the high resolution N1s spectra in Fig. S3. Upon the integration of Cu nanoparticles, there was a notable increment in the B-C configuration within the BNC-1 framework, this change attributed to the reduction of B-OH groups. This transformation was substantiated by the enhanced intensity of B-C peaks at 190.5 eV and the concurrent diminished intensity of B-O peaks at 192.3 eV, as evidenced in the high-resolution B1s spectra showcased in Fig. 1k. In the high-resolution C1s spectra in Fig. 1l, compared to the BNC-1, the Cu/BNC-1 showed the enhanced C-B (284.3 eV) and C-B (285.6 eV) intensity, further suggesting the Cu nanoparticles loading progress leading to more B, N dopants.

3.2. Electrochemical characterization

The CO_2RR performance was evaluated in CO_2-saturated 0.5 M $KHCO_3$ electrolyte in a three-electrode system in flow cell (Fig. S4). The linear sweep voltammetry (LSV) curves confirmed that the Cu/BNC-1 showed better catalytic activity than other control catalysts with lower onset potential and higher current density in Fig. 2a. The LSV curves comparison indicated that the specific carbon support of BNC-1 improved the catalytic activity of Cu nanoparticles. The liquid and gaseous products were detected by ^{1}H nuclear magnetic resonance (NMR) spectroscopy and on-line gas chromatography (GC), respectively. Fig. 2b displayed the products distribution of Cu/BNC-1 in CO_2RR on various potentials from −0.8 V to −1.2 V vs. RHE. At −0.8 V vs. RHE, H_2 and HCOOH are the main products, and EtOH (FE 6.47 %) started to formed as reported in the previous research [6]. Then, the FE of EtOH increases, and the maximum FE of EtOH is located at −1.0 V vs. RHE with the FE of 58.64 % and a partial current density of 20.4 mAcm^{-2} in Fig. 2c. We further compared the H_2, C_1 and C_2 products distribution with the control catalysts in Fig. 2d. Compared with Cu/BNC-1, the Cu/BNC-2 selectively shifted to CO and HCOOH with total FE around 70 %, and the FE of EtOH was significantly reduced. The CuN_4 favored to the production of CO and HCOOH with a total FE around 80 %, and no EtOH was detected. The BNC-1 exhibited a highest CO FE of 78.03 %. The results suggested that BNC-1 was effective in improving the selectivity of EtOH as a carbon carrier for Cu catalysts.

The electrochemically active surface area (ECSA) was measured to elucidate possible reasons for the CO_2RR activity of the Cu/BNC-1. The slopes of the scan rate and current density corresponding to the ECSA values were calculated from the measured values of the double-layer capacitance (Fig. S5). The calculated ECSA of Cu/BNC-1, Cu/BNC-2, CuN_4 and BNC-1 were quantified by 45, 18, 0.3 and 5.7 mF cm^{-2}, respectively. The ECSA calculations suggested that the Cu/BNC-1 had a higher ECSA value, indicating a denser presence of catalytic active sites available for reactions. The cathodic energy efficiency (EE) was determined to assess the energy conversion efficiency specifically for EtOH production. The superior catalytic performance of Cu/BNC-1 for CO_2
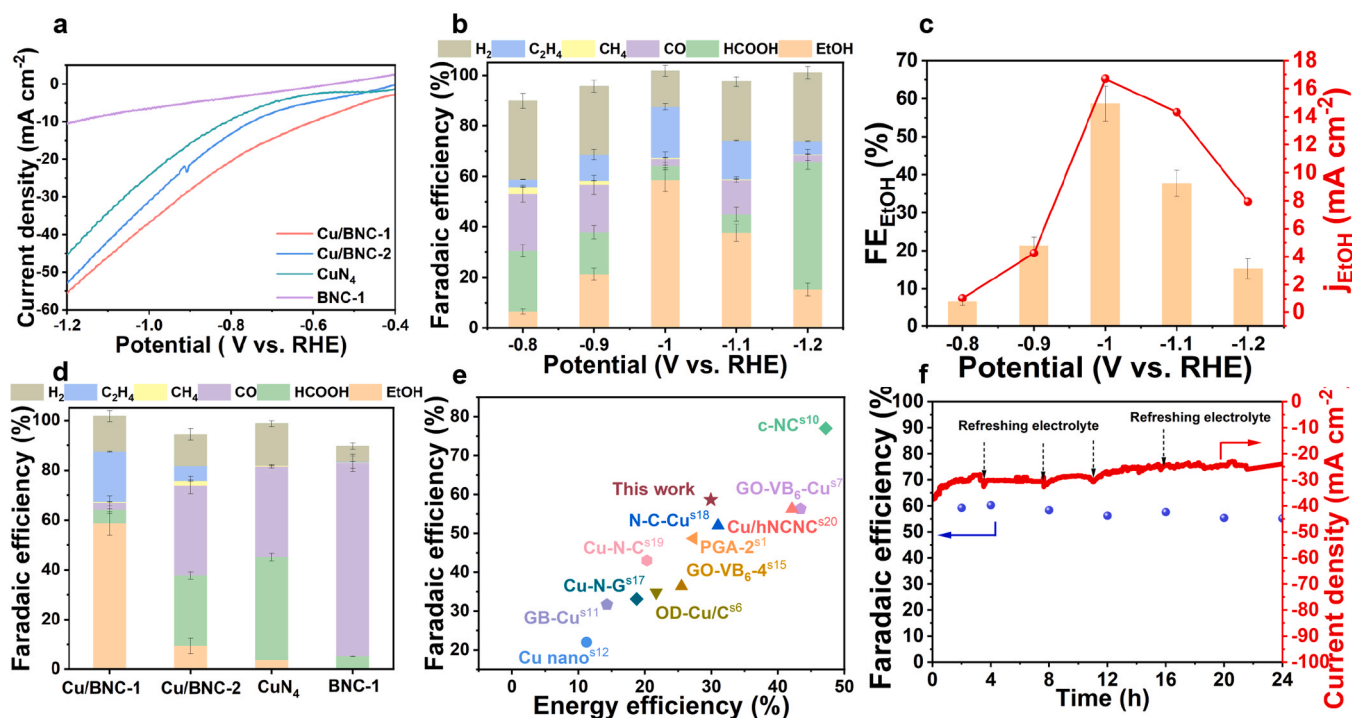
Fig. 2. (a) The LSV curves of four samples in CO_2-saturated electrolyte. (b) The faraday efficiencies (FE) of Cu/BNC-1 at the range from −0.8 V to −1.2 V vs. RHE. (c) The FE_{EtOH} of Cu/BNC-1 at the range from −0.8 V to −1.2 V vs. RHE. (d) The FE for four samples at −1.0 V vs. RHE. (e) The activity comparison (EE_{EtOH} and FE_{EtOH}) with reported electrocatalysts. (f) The FE and current density stability of Cu/BN-C-1 during continuous 24-h testing.

reduction to EtOH was compared to the reported electrocatalysts in term of two key indicators (FE and EE) in Fig. 2e and Table S1. In the axis of EE-FE, the Cu/BNC-1 was located at upper right area, confirming the superior CO_2RR performance for producing high valuable EtOH. Compared the reported stability tests within 12 h, a longer-term (24 h) durability and selectivity of Cu/BNC-1 was measured in Fig.2 f, and almost no changed EtOH FE and lightly decreased current density demonstrated the excellent catalytic stability.

In order to explore the mechanism of stable catalytic performance in Cu/BNC-1, the morphology and valance state of Cu nanoparticles were characterized by HR-TEM and XPS techniques. The diameter size changes of Cu nanoparticles after 8 h, 16 h, 24 h electrocatalysis at −1.0 V vs. RHE in Fig. 3a-d demonstrated a progressive decrease in the diameter size of the Cu nanoparticles as time advances. Initially, the Cu nanoparticles exhibited an average diameter size of approximately 100 nm without applying potential. Upon the application of electricity for a duration of 8 h, there was a notable reduction in particle size to the range of 35–40 nm. This trend continued, with a further decrease to 30–35 nm after 16 h of continuous energization. After 24 h, the Cu nanoparticles attained a significantly reduced diameter size of 8–16 nm. These findings suggested a time-dependent diameter size refinement of Cu nanoparticles under the influence of electrical energy. The EDS elemental maps of Cu (Fig. 3e-h) further verified the Cu nanoparticles diminished in diameter size as the duration of energization extends. This analytical technique provides additional verification of the time-dependent reduction in particle size, aligning with the progressive energization timeline. As shown in Fig. 2f, the catalytic action of Cu nanoparticles in the CO_2RR was not compromised by changes in their dimensions. This indicated that the reduction in diameter size of Cu nanoparticles, coupled with the emergence of new active sites, compensated for any loss in activity, thereby maintaining the catalytic performance.

As demonstrated by the XPS of Cu at different times, the relatively strong peak for Cu^0/Cu^+ indicated that Cu^0/Cu^+ was the predominant form present before CO_2RR. As the CO_2RR proceeded, Cu was reduced

from the Cu^{2+} or Cu^+ to the Cu^0 [35]. This process may be accompanied by adsorption and activation of CO_2, leading to the formation of intermediates [36,37]. After the CO_2RR, the surface of the Cu may change due to the interaction with the reaction products and intermediates [38–41]. The phenomenon has been reported in many papers that with the increasing time under applying negative potential, the large-size metal nanoparticles were decomposed into small-size nanoparticles or even single metal atoms, which were then immobilized and coordinated with the doped heteroatom atoms in the carbon matrix [42,43]. Cu oxidation state changes can be observed from high-resolution Cu spectra, which were more susceptible to oxidation when the Cu nanoparticles were small and had a higher proportion of unsatisfied valence electrons in the surface atoms compared to larger particles. The oxidation state of Cu played a crucial role in determining the product distribution. It was found that the morphological evolution, alongside shifts in the oxidation state as observed through XPS analysis, indicating a dynamic restructuring process that potentially enhanced the activity and selectivity towards CO_2RR, particularly favoring the production of EtOH.

3.3. In situ measurements and DFT calculations

To elucidate the possible reaction mechanism of CO_2-to-EtOH conversion, *in-situ* Raman spectra and *in-situ* IR spectra were applied on Cu/BNC-1 to detect the reaction intermediates. Fig. 4a-b showed the *in-situ* Raman spectra and *in-situ* IR spectra, respectively. At the open-circuit potential (OCP), the Cu/BNC-1 electrode exhibited two significant Raman signals located at approximately 1350 and 1580 cm^{-1}, respectively, which correspond exactly to the D and G bands of substrate BNC [44]. The results of potential-dependent spectroscopy covering a potential window from the OCP to - 0.8 V vs. RHE showed that the signal was located at 1068 cm^{-1}, which can be attributed to the stretching mode of the adsorbed carbonate in the interfacial region (CO_3^{2-} symmetric stretching mode) [45]. At the same time, a peak associated with *CO (C≡O stretching), a necessary intermediate for C≡C coupling, was
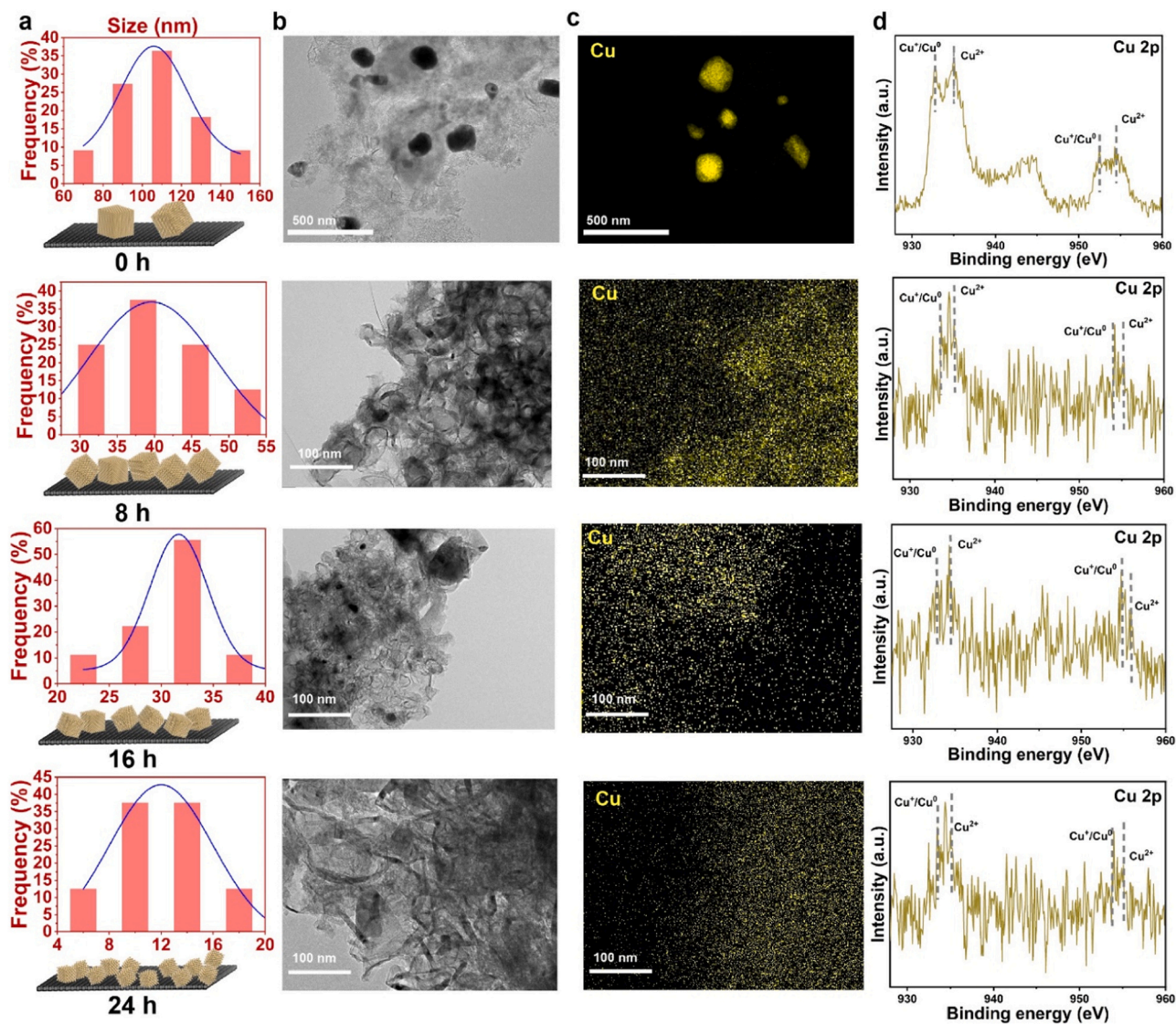
Fig. 3. (a) The schematic illustrating of the evolution of Cu nanoparticle size and corresponding particle size distribution for Cu/BNC-1 without CO_2RR and after 8 h, 16 h, 24 h of CO_2RR, respectively. (b) TEM image for Cu/BNC-1 without $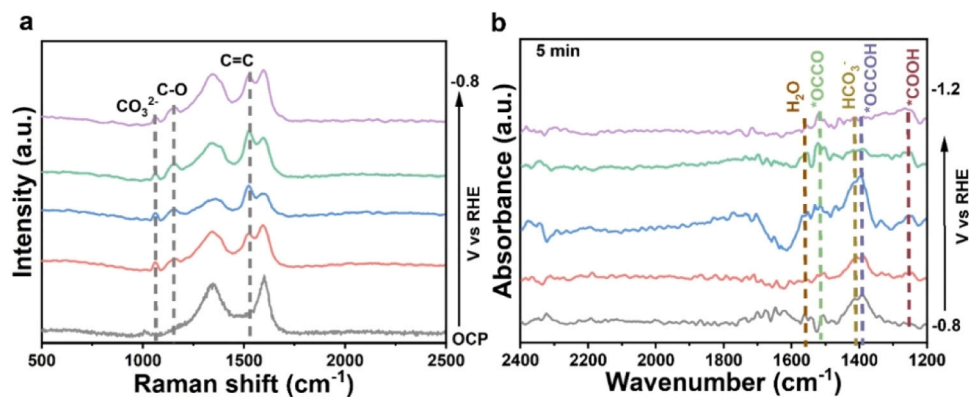CO_2RR$ and after 8 h, 16 h, 24 h of CO_2RR, respectively. (c) EDS elemental mapping for Cu/BNC-1 without CO_2RR and after 8 h, 16 h, 24 h of CO_2RR, respectively. (d) Cu 2p XPS spectra for Cu/BNC-1 without CO_2RR and after 8 h, 16 h, 24 h of CO_2RR, respectively.

Fig. 4. (a) *In-situ* Raman spectroscopic study in CO_2-saturated 0.5 M $KHCO_3$ solution on Cu/BNC-1. (b) *In-situ* IR analysis n CO_2-saturated 0.5 M $KHCO_3$ solution on Cu/BNC-1.

also observed at 2064 cm^{-1}. The signal at 1550 cm^{-1} represented C=C symmetric stretching in the Cu/BNC-1, indicating successful C=C coupling and EtOH formation [46]. As can see from Fig. 4b and Fig. S6-10, with increasing bias potentials, the IR spectra displayed three bands at 1560 and 1458 and 1280 cm^{-1} after 5 min of CO$_2$RR. The bands near 1560 cm^{-1} were assigned as a CO vibrational frequency (νCO) of a C$_2$ intermediate species, νCO in *OCCO was 1553 cm^{-1}, and νCO of *OCCOH was 1458 cm^{-1}. The band at around 1288 cm^{-1} was mainly ascribed to the stretching vibration of *COOH. *COOH served as an important intermediate in the conversion of CO$_2$ to CO, facilitated through a mechanism involving coupled proton-electron transfer. Furthermore, *CO is a crucial intermediate in the synthesis of C$_2$ products [47]. *CO initially underwent dimerization forming *OCCO. This intermediate then participated in protonation and dehydration steps, converting into *OCCOH. *OCCOH served as a common precursor for the synthesis of both C$_2$H$_4$ and CH$_3$CH$_2$OH [48–50]. Subsequently, *OCCOH leaded to C$_2$H$_4$ through deoxygenation and protonation processes, or it directly converted into CH$_3$CH$_2$OH via a protonation reaction. Integrating the in-situ FTIR findings, the detection of *OCCO and *OCCOH signals revealed the formation of CH$_2$CHO and CH$_3$CHO intermediates within the reaction [51,52]. These intermediates played a pivotal role in the concurrent formation of CH$_3$CH$_2$OH.

To gain more fundamental insights, DFT calculations were performed for disclosing the origin of Cu/BNC-1 performance toward CO$_2$RR to EtOH at atomic levels. We investigated the CO dimerization reaction (Fig. 5a-c and Fig. S11 and 12), a key step for C$_{2+}$ production, on three different models, namely B, N doping graphene layer on the Cu surface (Cu/BNC-1), a B, N doping amorphous carbon layer on the Cu surface (Cu/BNC-2) and Cu only. The distances between carbon-based layer and the Cu were set in the range of 6–9 Å based on literature

results, which shows EtOH selectivity promotion on Cu/NC [14]. The calculated reaction energies for C-C coupling was shown in Fig. 5d. The Cu/BNC-1 had the lowest barrier and enthalpy change for CO dimerization compared to Cu/BNC-2 and Cu, suggesting that the Cu/BNC-1 was likely to deliver the highest selectivity to C$_{2+}$ products. To understand how the BNC layer affects CO dimerization, we also generated electron density difference plots for Cu/BNC-1, Cu/BNC-2 and Cu with two adsorbed *CO intermediates in solution (Fig. S13). The BNC-1 layer lost electrons (blue) and the adsorbed *CO gained electrons (yellow), whereas there was no obvious electron transfer between the carbon layer and the adsorbed *CO, suggesting that the BNC-1 layer was beneficial to electron transfer to adsorbed *CO on Cu, and that it thus promoted the generation of the C-C coupled intermediate.

*HOCCH is the key intermediate from which branches the ethylene pathway and the EtOH pathway (Fig. S14), we therefore further calculated the reaction energies of *HOCCH to *CCH (ethylene pathway) and *HOCCH to *HOCHCH (EtOH pathway) to understand the effect of different confining materials on the C$_2$ product distribution [9,11]. Compared to bare Cu, the Cu/BNC-1 catalysts improved EtOH selectivity versus ethylene (Fig. 5e and Fig. S15-17), which was ascribed to the confinement effect in the stabilization of the C-O bond of *HOCCH, leading to a suppression of the deoxygenation process [8,14]. The Cu/BNC-2 catalyst did not enhance the selectivity for EtOH over ethylene when compared to the performance of bare Cu. This observation implied that the inhibition of C-O bond cleavage by the *HOCCH intermediate was exclusive to the crystalline form of Cu/BNC. Consequently, these findings pointed to the crystalline Cu/BNC as a promising candidate with the potential for heightened selectivity towards EtOH production.
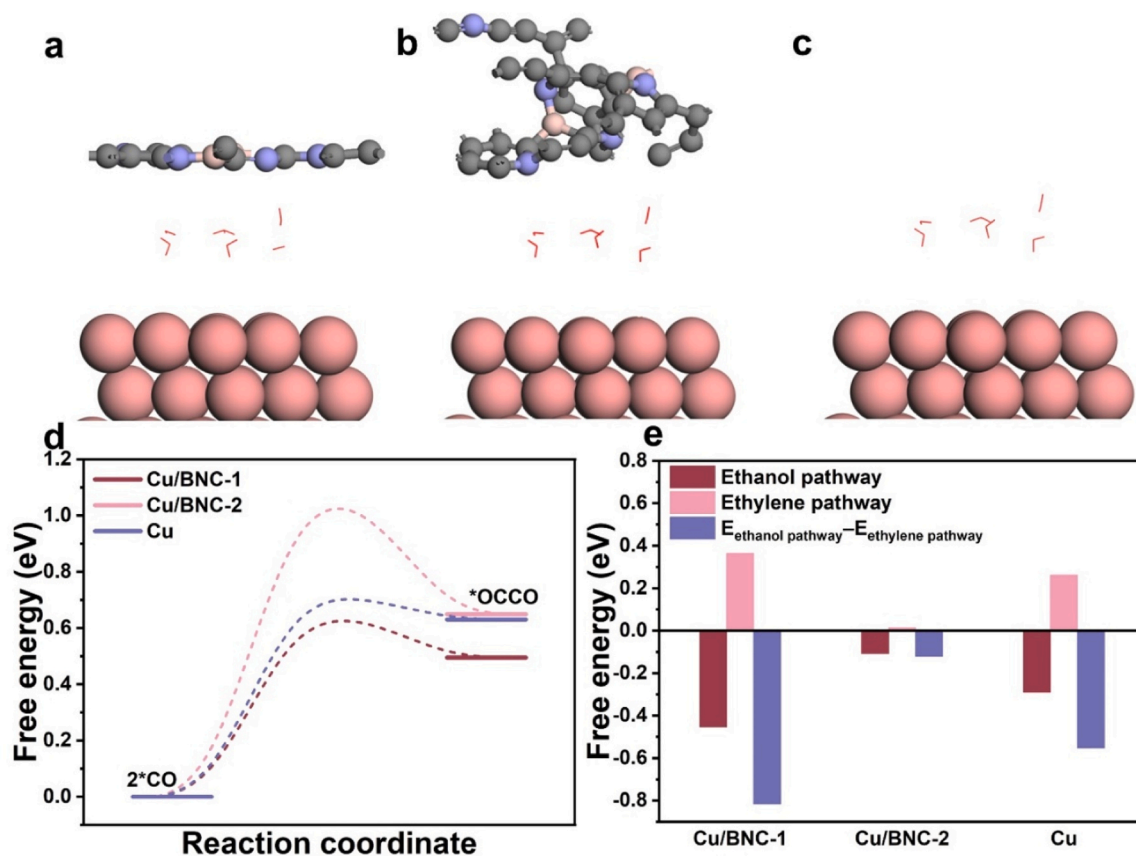

Fig. 5. DFT calculation models of (a) Cu/BNC-1; (b) Cu/BNC-2; (c) Cu. (e) Energy barriers of the dimerization of two *CO at both atop sites and two *CO on Cu/BNC-1, Cu/BNC-2 and Cu, respectively. IS, initial state; TS, transient state; and FS, final state. (f) Reaction energies of the ethylene pathway (*HOCCH to *CCH) and the ethanol pathway (*HOCCH to *HOCHCH) on Cu/BNC-1, Cu/BNC-2 and Cu.

4. Conclusions

In conclusion, our study successfully synthesized Cu nanoparticles on Cu/BNC-1, which exhibited outstanding catalytic performance in CO_2 reduction to EtOH. This catalyst demonstrated a high Faradaic efficiency of 58.64 % at −1.0 V vs. RHE and maintained substantial stability with 55 % FE over 24 h, outperforming traditional carbon-supported Cu catalysts. The durability tests highlighted the vital role of pyridinic N-B sites in modulating the electronic structure of Cu. *In-situ* Raman, FT-IR spectroscopy, and DFT calculations demonstrated that Cu/BNC-1 significantly enhanced C_{2+} product selectivity, favoring EtOH production over ethylene. This was due to its lowered CO dimerization barrier and the stabilizing effect of its crystalline structure on the C-O bond in the *HOCCH intermediate.

CRediT authorship contribution statement

Mengmeng Fan: Writing – review & editing, Supervision, Conceptualization. **Jianchun Jiang:** Writing – review & editing, Supervision, Conceptualization. **Ziyun Wang:** Writing – review & editing, Supervision, Conceptualization. **Ao Wang:** Formal analysis. **Kang Sun:** Formal analysis. **Chenhao Zhang:** Formal analysis. **Qixin Yuan:** Formal analysis. **Yuying Zhao:** Writing – review & editing, Writing – original draft, Methodology, Investigation. **Ruting Xu:** Investigation. **Anqi Zhang:** Formal analysis.

Declaration of Competing Interest

Data availability

Data will be made available on request.

Acknowledgements

Appendix A. Supporting information

Supplementary data associated with this article can be found in the online version at doi:10.1016/j.apcatb.2024.124168.

References

[1] Y. Zhao, Q. Yuan, M. Fan, A. Wang, K. Sun, Z. Wang, J. Jiang, Fabricating pyridinic N-B sites in porous carbon as efficient metal-free electrocatalyst in conversion CO_2 into CH_4, Chin. Chem. Lett. 34 (2022) 108120.

[2] K. Yao, H. Wang, X. Yang, Y. Huang, C. Kou, T. Jing, S. Chen, Z. Wang, Y. Liu, H. Liang, Metal-organic framework derived dual-metal sites for electroreduction of carbon dioxide to HCOOH, Appl. Catal. B 311 (2022) 121377.

[3] Y. Zhao, J. Raj, X. Xu, J. Jiang, J. Wu, M. Fan, Carbon catalysts empowering sustainable chemical synthesis via electrochemical CO_2 conversion and two-electron oxygen reduction reaction, Small (2024) e2311163.

[4] T.C. Chou, C.C. Chang, H.L. Yu, W.Y. Yu, C.L. Dong, J.J. Velasco-Velez, C. H. Chuang, L.C. Chen, J.F. Lee, J.M. Chen, H.L. Wu, Controlling the oxidation state of the Cu electrode and reaction intermediates for electrochemical CO_2 reduction to ethylene, J. Am. Chem. Soc. 142 (2020) 2857–2867.

[5] A. Vasileff, Y. Zhu, X. Zhi, Y. Zhao, L. Ge, H.M. Chen, Y. Zheng, S.Z. Qiao, Electrochemical reduction of CO_2 to ethane through stabilization of an ethoxy intermediate, Angew. Chem. Int. Ed. 59 (2020) 19649–19653.

[6] X. Su, Z. Jiang, Z. Zhou, H. Liu, D. Zhou, H. Shang, X. Ni, Z. Peng, F. Yang, W. Chen, Z. Qi, D. Wang, Y. Wang, Complementary operando spectroscopy identification of in-situ generated metastable charge-asymmetry Cu_2-CuN_3 clusters for CO_2 reduction to ethanol, Nat. Commun. 13 (2022) 1322.

[7] K. Qi, Y. Zhang, N. Onofrio, E. Petit, X. Cui, J. Ma, J. Fan, H. Wu, W. Wang, J. Li, J. Liu, Y. Zhang, Y. Wang, G. Jia, J. Wu, L. Lajaunie, C. Salameh, D. Voiry, Unlocking direct CO_2 electrolysis to C_3 products via electrolyte supersaturation, Nat. Catal. 6 (2023) 319–331.

[8] G.M. Tomboc, S. Choi, T. Kwon, Y.J. Hwang, K. Lee, Potential link between Cu surface and selective CO_2 electroreduction: perspective on future electrocatalyst designs, Adv. Mater. 32 (2020) e1908398.

[9] D. Zang, X.J. Gao, L. Li, Y. Wei, H. Wang, Confined interface engineering of self-supported Cu@N-doped graphene for electrocatalytic CO_2 reduction with enhanced selectivity towards ethanol, Nano Res. 15 (2022) 8872–8879.

[10] D. Karapinar, N.T. Huan, N. Ranjbar Sahraie, J. Li, D. Wakerley, N. Touati, S. Zanna, D. Taverna, L.H. Galvao Tizei, A. Zitolo, F. Jaouen, V. Mougel, M. Fontecave, Electroreduction of CO_2 on single-site copper-nitrogen-doped carbon material: selective formation of ethanol and reversible restructuration of the metal sites, Angew. Chem. Int. Ed. 58 (2019) 15098–15103.

[11] L.R.L. Ting, O. Piqué, S.Y. Lim, M. Tanhaei, F. Calle-Vallejo, B.S. Yeo, Enhancing CO_2 electroreduction to ethanol on copper-silver composites by opening an alternative catalytic pathway, ACS Catal. 10 (2020) 4059–4069.

[12] X. Wang, P. Ou, J. Wicks, Y. Xie, Y. Wang, J. Li, J. Tam, D. Ren, J.Y. Howe, Z. Wang, A. Ozden, Y.Z. Finfrock, Y. Xu, Y. Li, A.S. Rasouli, K. Bertens, A.H. Ip, M. Graetzel, D. Sinton, E.H. Sargent, Gold-in-copper at low *CO coverage enables efficient electromethanation of CO_2, Nat. Commun. 12 (2021) 3387.

[13] J. Feng, L. Zhang, S. Liu, L. Xu, X. Ma, X. Tan, L. Wu, Q. Qian, T. Wu, J. Zhang, X. Sun, B. Han, Modulating adsorbed hydrogen drives electrochemical CO_2-to-C_2 products, Nat. Commun. 14 (2023) 4615.

[14] X. Wang, Z. Wang, F.P. García de Arquer, C.-T. Dinh, A. Ozden, Y.C. Li, D.-H. Nam, J. Li, Y.-S. Liu, J. Wicks, Z. Chen, M. Chi, B. Chen, Y. Wang, J. Tam, J.Y. Howe, A. Proppe, P. Todorović, F. Li, T.-T. Zhuang, C.M. Gabardo, A.R. Kirmani, C. McCallum, S.-F. Hung, Y. Lum, M. Luo, Y. Min, A. Xu, C.P. O'Brien, B. Stephen, B. Sun, A.H. Ip, L.J. Richter, S.O. Kelley, D. Sinton, E.H. Sargent, Efficient electrically powered CO_2-to-ethanol via suppression of deoxygenation, Nat. Energy 5 (2020) 478–486.

[15] Y. Zhao, Q. Yuan, K. Sun, A. Wang, R. Xu, J. Xu, Y. Wang, M. Fan, J. Jiang, Curvature effect of pyridinic N-modified carbon atom sites for electrocatalyzing CO_2 conversion to CO, ACS Appl. Mater. Interf. 15 (2023) 37593–37601.

[16] Q. Chang, Y. Liu, J.-H. Lee, D. Ologunagba, S. Hwang, Z. Xie, S. Kattel, J.H. Lee, J. G. Chen, Metal-coordinated phthalocyanines as platform molecules for understanding isolated metal sites in the electrochemical reduction of CO_2, J. Am. Chem. Soc. 144 (2022) 16131–16138.

[17] S. Navarro-Jaen, M. Virginie, J. Bonin, M. Robert, R. Wojcieszak, A.Y. Khodakov, Highlights and challenges in the selective reduction of carbon dioxide to methanol, Nat. Rev. Chem. 5 (2021) 564–579.

[18] Y. Song, P. Guo, T. Ma, J. Su, L. Huang, W. Guo, Y. Liu, G. Li, Y. Xin, Q. Zhang, S. Zhang, H. Shen, X. Feng, D. Yang, J. Tian, S.K. Ravi, B.Z. Tang, R. Ye, Ultrathin, cationic covalent organic nanosheets for enhanced CO_2 electroreduction to methanol, Adv. Mater. (2023) 2310037.

[19] J. Su, C.B. Musgrave, Y. Song, L. Huang, Y. Liu, G. Li, Y. Xin, P. Xiong, M.M.-J. Li, H. Wu, M. Zhu, H.M. Chen, J. Zhang, H.M. Shen, B.Z. Tang, M. Robert, W.A. Goddard, R. Ye, Strain enhances the activity of molecular electrocatalysts via carbon nanotube supports, Nat. Catal. 6 (2023) 818–828.

[20] H. Yang, Y. Wu, Q. Lin, L. Fan, X. Chai, Q. Zhang, J. Liu, C. He, Z. Lin, Composition tailoring via N and S Co-doping and structure tuning by constructing hierarchical pores: metal-free catalysts for high-performance electrochemical reduction of CO_2, Angew. Chem. Int. Ed. 57 (2018) 15476–15480.

[21] D. Hursán, A.A. Samu, L. Janovák, K. Artyushkova, T. Asset, P. Atanassov, C. Janáky, Morphological attributes govern carbon dioxide reduction on N-doped carbon electrodes, Joule 3 (2019) 1719–1733.

[22] C. Chen, X. Yan, S. Liu, Y. Wu, Q. Wan, X. Sun, Q. Zhu, H. Liu, J. Ma, L. Zheng, H. Wu, B. Han, Highly efficient electroreduction of CO_2 to C_{2+} alcohols on heterogeneous dual active sites, Angew. Chem. Int. Ed. 59 (2020) 16459–16464.

[23] D. Karapinar, N.T. Huan, N. Ranjbar Sahraie, J. Li, D. Wakerley, N. Touati, S. Zanna, D. Taverna, L.H. Galvão Tizei, A. Zitolo, F. Jaouen, V. Mougel, M. Fontecave, Electroreduction of CO_2 on single-site copper-nitrogen-doped carbon

material: selective formation of ethanol and reversible restructuration of the metal sites, Angew. Chem. Int. Ed. 58 (2019) 15098–15103.

[24] F. Abild-Pedersen, J. Greeley, F. Studt, J. Rossmeisl, T.R. Munter, P.G. Moses, E. Skulason, T. Bligaard, J.K. Norskov, Scaling properties of adsorption energies for hydrogen-containing molecules on transition-metal surfaces, Phys. Rev. Lett. 99 (2007) 016105.

[25] A.A. Peterson, F. Abild-Pedersen, F. Studt, J. Rossmeisl, J.K. Nørskov, How copper catalyzes the electroreduction of carbon dioxide into hydrocarbon fuels, Energy Environ. Sci. 3 (2010) 1311–1315.

[26] M.T.M. Koper, Thermodynamic theory of multi-electron transfer reactions: Implications for electrocatalysis, J. Electroanal. Chem. 660 (2011) 254–260.

[27] M.T.M. Koper, Theory of multiple proton-electron transfer reactions and its implications for electrocatalysis, Chem. Sci. 4 (2013) 2710.

[28] M. Fan, Q. Yuan, Y. Zhao, Z. Wang, A. Wang, Y. Liu, K. Sun, J. Wu, L. Wang, J. Jiang, A Facile "Double-Catalysts" Approach to Directionally Fabricate Pyridinic N-B-Pair-Doped Crystal Graphene Nanoribbons/Amorphous Carbon Hybrid Electrocatalysts for Efficient Oxygen Reduction Reaction, Adv. Mater. 34 (2022) e2107040.

[29] J. Zhang, Z. Li, R. Cai, T. Zhang, S. Yang, L. Ma, Y. Wang, Y. Wu, J. Wu, Switching CO_2 electroreduction selectivity between C1 and C2 hydrocarbons on Cu gas-diffusion electrodes, Energy Environ. Sci. 6 (2023) e12307.

[30] H. Jung, S.Y. Lee, C.W. Lee, M.K. Cho, D.H. Won, C. Kim, H.-S. Oh, B.K. Min, Y. J. Hwang, Electrochemical fragmentation of Cu_2O nanoparticles enhancing selective C–C coupling from CO_2 reduction reaction, J. Am. Chem. Soc. 141 (2019) 4624–4633.

[31] Y. Zhao, X. Xu, Q. Yuan, Y. Wu, K. Sun, B. Li, Z. Wang, A. Wang, H. Sun, M. Fan, J. Jiang, Interfacial engineering of a vertically stacked graphene/h-BN heterostructure as an efficient electrocatalyst for hydrogen peroxide synthesis, Mater. Horiz. 10 (2023) 4930–4939.

[32] Y. Wu, Q. Yuan, Y. Zhao, X. Xu, J. Xu, Y. Wang, K. Sun, A. Wang, H. Sun, B. Li, R. Xu, Z. Wang, J. Jiang, M. Fan, Boron–sulfur pairs for highly active 2e⁻ oxygen reduction reaction to electrochemically synthesize hydrogen peroxide, ACS Sustain. Chem. Eng. 11 (2023) 13363–13373.

[33] M.W. Fan, Zeming, Kang Sun, Ao Wang, Yuying Zhao, Qixin Yuan, R.R. Wang, Jitu, Wu Jingjie, Jianchun Jiang, Liang Wang, N-B-OH site-activated graphene quantum dots for boosting electrochemical hydrogen peroxide production, Adv. Mater. 35 (2023) e2209086.

[34] M. Fan, Z. Wang, Y. Zhao, Q. Yuan, J. Cui, J. Raj, K. Sun, A. Wang, J. Wu, H. Sun, B. Li, L. Wang, J. Jiang, Porous heterostructure of graphene/hexagonal boron nitride as an efficient electrocatalyst for hydrogen peroxide generation, Carbon Energy 5 (2022) e309.

[35] J. Wang, H.Y. Tan, Y. Zhu, H. Chu, H.M. Chen, Linking the dynamic chemical state of catalysts with the product profile of electrocatalytic CO_2 reduction, Angew. Chem. Int. Ed. 60 (2021) 17254–17267.

[36] Y. Chen, Z. Fan, J. Wang, C. Ling, W. Niu, Z. Huang, G. Liu, B. Chen, Z. Lai, X. Liu, B. Li, Y. Zong, L. Gu, J. Wang, X. Wang, H. Zhang, Ethylene selectivity in electrocatalytic CO_2 reduction on Cu nanomaterials: a crystal phase-dependent study, J. Am. Chem. Soc. 142 (2020) 12760–12766.

[37] F. Cavalca, R. Ferragut, S. Aghion, A. Eilert, O. Diaz-Morales, C. Liu, A.L. Koh, T. W. Hansen, L.G.M. Pettersson, A. Nilsson, Nature and distribution of stable subsurface oxygen in copper electrodes during electrochemical CO_2 reduction, J. Phys. Chem. C 121 (2017) 25003–25009.

[38] V. Okatenko, A. Loiudice, M.A. Newton, D.C. Stoian, A. Blokhina, A.N. Chen, K. Rossi, R. Buonsanti, Alloying as a strategy to boost the stability of copper nanocatalysts during the electrochemical CO_2 reduction reaction, J. Am. Chem. Soc. 145 (2023) 5370–5383.

[39] Y. Li, W. Hong, S. Chen, R. Duan, S. Chai, W. Du, J. Yang, J. Mao, Correlating the valence state of a Cu-based electrocatalyst for CO_2 reduction to C_2, Chem. Commun. 59 (2023) 11716–11719.

[40] J.-N. Lu, J. Liu, L. Zhang, L.-Z. Dong, S.-L. Li, Y.-Q. Lan, Crystalline mixed-valence copper supramolecular isomers for electroreduction of CO_2 to hydrocarbons, J. Mater. Chem. A 9 (2021) 23477–23484.

[41] A.R. Woldu, Z. Huang, P. Zhao, L. Hu, D. Astruc, Electrochemical CO_2 reduction (CO_2RR) to multi-carbon products over copper-based catalysts, Coord. Chem. Rev. 454 (2022) 214340.

[42] P. De Luna, R. Quintero-Bermudez, C.-T. Dinh, M.B. Ross, O.S. Bushuyev, P. Todorović, T. Regier, S.O. Kelley, P. Yang, E.H. Sargent, Catalyst electro-redeposition controls morphology and oxidation state for selective carbon dioxide reduction, Nat. Catal. 1 (2018) 103–110.

[43] Y.X. Duan, F.L. Meng, K.H. Liu, S.S. Yi, S.J. Li, J.M. Yan, Q. Jiang, Amorphizing of Cu nanoparticles toward highly efficient and robust electrocatalyst for CO_2 reduction to liquid fuels with high faradaic efficiencies, Adv. Mater. 30 (2018) e1706194.

[44] F. Yang, C. Liang, H. Yu, Z. Zeng, Y.M. Lam, S. Deng, J. Wang, Phosphorus-doped graphene aerogel as self-supported electrocatalyst for CO_2-to-ethanol conversion, Adv. Sci. 9 (2022) e2202006.

[45] S. Mu, H. Lu, Q. Wu, L. Li, R. Zhao, C. Long, C. Cui, Hydroxyl radicals dominate reoxidation of oxide-derived Cu in electrochemical CO_2 reduction, Nat. Commun. 13 (2022) 3694.

[46] W. Xia, Y. Xie, S. Jia, S. Han, R. Qi, T. Chen, X. Xing, T. Yao, D. Zhou, X. Dong, J. Zhai, J. Li, J. He, D. Jiang, Y. Yamauchi, M. He, H. Wu, B. Han, Adjacent copper single atoms promote C-C coupling in electrochemical CO_2 reduction for the efficient conversion of ethanol, J. Am. Chem. Soc. 145 (2023) 17253–17264.

[47] M. Dunwell, Y. Yan, B. Xu, In situ infrared spectroscopic investigations of pyridine-mediated CO_2 reduction on Pt electrocatalysts, ACS Catal. 7 (2017) 5410–5419.

[48] S. Zhu, B. Jiang, W.B. Cai, M. Shao, Direct observation on reaction intermediates and the role of bicarbonate anions in CO_2 electrochemical reduction reaction on Cu surfaces, J. Am. Chem. Soc. 139 (2017) 15664–15667.

[49] Y. Katayama, F. Nattino, L. Giordano, J. Hwang, R.R. Rao, O. Andreussi, N. Marzari, Y. Shao-Horn, An in situ surface-enhanced infrared absorption spectroscopy study of electrochemical CO_2 reduction: selectivity dependence on surface C-bound and O-bound reaction intermediates, J. Phys. Chem. C 123 (2018) 5951–5963.

[50] T. Cheng, A. Fortunelli, W.A. Goddard 3rd, Reaction intermediates during operando electrocatalysis identified from full solvent quantum mechanics molecular dynamics, Proc. Natl. Acad. Sci. USA 116 (2019) 7718–7722.

[51] Y. Kim, S. Park, S.-J. Shin, W. Choi, B.K. Min, H. Kim, W. Kim, Y.J. Hwang, Time-resolved observation of C–C coupling intermediates on Cu electrodes for selective electrochemical CO_2 reduction, Energy Environ. Sci. 13 (2020) 4301–4311.

[52] X. Shen, X. Liu, S. Wang, T. Chen, W. Zhang, L. Cao, T. Ding, Y. Lin, D. Liu, L. Wang, W. Zhang, T. Yao, Synergistic modulation at atomically dispersed Fe/Au interface for selective CO_2 electroreduction, Nano Lett. 21 (2021) 686–692.